Directed Self-Assembly as a Route to Ferromagnetic and Superparamagnetic Nanoparticle Arrays

*Laura T. Schelhas, Richard A. Farrell, Udayabagya Halim, and Sarah H. Tolbert**

Block co-polymer patterns are attractive candidates for nanoparticle assemblies. Directed self-assembly of block co-polymers in particular allows for long range ordering of the patterns, making them interesting scaffolds for the organization of magnetic particles. Here, a method to tune the channel width of polymer-derived trenches via atomic layer deposition (ALD) of alumina is reported. The alumnia coating provides a much more thermally robust pattern that is stable up to 250 °C. Using these patterns, magnetic coupling in both ferromagnetic and superparamagnetic nanocrystal chains is achieved.

1. Introduction

Block co-polymer (BCP) systems have been gaining interest due to their ability to spontaneously assemble into a range of interesting morphologies.[1–3] These systems also provide access to sub 10 nm length scales that may not be possible with conventional lithographic techniques.[4–13] Cylindrical phase forming polymers are of particular interest as they are able to create holes, dots, or trenches depending on their orientation to the surface. Feature sizes and orientations are controlled by composition, wetting, and the molecular weight of the BCP. Additionally, nanopatterns can be produced with both orientational and positional control of the features when self-assembled block co-polymers are coupled with conventional lithography.[6,9,14–21]

Here, we combine these block co-polymer patterns with magnetic nanocrystals. Synthesis advancements in recent years now allow for increased size and composition control in magnetic nanoparticles.[22] This has been accompanied by increased efforts to find ways to organize these nanoparticles into arrays.[23–26] Magnetic nanoparticles are particularly interesting for organizational studies because the particles are able to magnetically couple when positioned close to each other.[24,25,27,28] We note that ordered magnetic nanocrystal arrays have been made previously using lithographic techniques, but these fabrication techniques are expensive and the array area is small.[29,30] There have also been some previous reports of organized nanoparticles using BCP; but in general these previous systems have been composed of non-interacting nanoparticles.[31–35] We note that non-noble metal nanoparticles, in particular, are very sensitive to oxidative reactions with the substrate, even when kept in inert conditions, and so to create interacting arrays of these nanoparticles, the top layer of the pattern must be carefully controlled.

One interesting magnetic nanoparticle system is iron-platinum (FePt). The magnetic properties of FePt can be tuned not only by size but also by composition and by the nanoparticle crystal structure. FePt with a 1:1 atomic ratio is of particular interest because it can exist in two different crystal structures. Its random face centered cubic (fcc) phase is superparamagnetic. Superparamagnetism occurs in nanoscale ferromagnetic crystals when the ambient thermal energy is larger than the magnetocrystalline anisotropy resulting in a material that responds to a magnetic field but shows zero net magnetization without the presence of a magnetic field. Conversely, through thermal annealing, the crystal structure of the FePt can be converted to the ordered intermetallic face centered tetragonal (fct) phase.[26,36–38] The fct phase has very large magnetocrystalline anisotropy, and so fct FePt is ferromagnetic even on size scales as small as 3.5 nm diameter.[39] For these reasons FePt is expected to have possible applications in high-density data storage.[38,40,41]

Here we report experimental results demonstrating that block co-polymers when combined with a directed self-assembly approach can provide high-density arrays of aligned nanopatterns with critical dimensions smaller than those achievable using conventional lithography. We also show that these patterns can be used to organize functional nanoparticles by controlling the precise dimensions surface of the patterns.

Dr. L. T. Schelhas, Dr. R. A. Farrell, U Halim, Prof. S. H. Tolbert
Department of Chemistry and Biochemistry
University of California Los Angeles (UCLA)
Los Angeles, CA 90095, USA
E-mail: Tolbert@chem.ucla.edu
Prof. S. H. Tolbert
Department of Materials Science and Engineering
University of California Los Angeles (UCLA)
Los Angeles, CA 90095, USA
Prof. S. H. Tolbert
California NanoSystems Institute
University of California Los Angeles (UCLA)
Los Angeles, CA 90095, USA

DOI: 10.1002/adfm.201401921

2. Results and Discussion

2.1. Self-Assembly and ALD

In this work, we make use of a poly(styrene-*b*-dimethyl siloxane) (PS-*b*-PDMS) diblock co-polymer. The polymer is deposited on top of an OH-terminated PDMS polymer, which

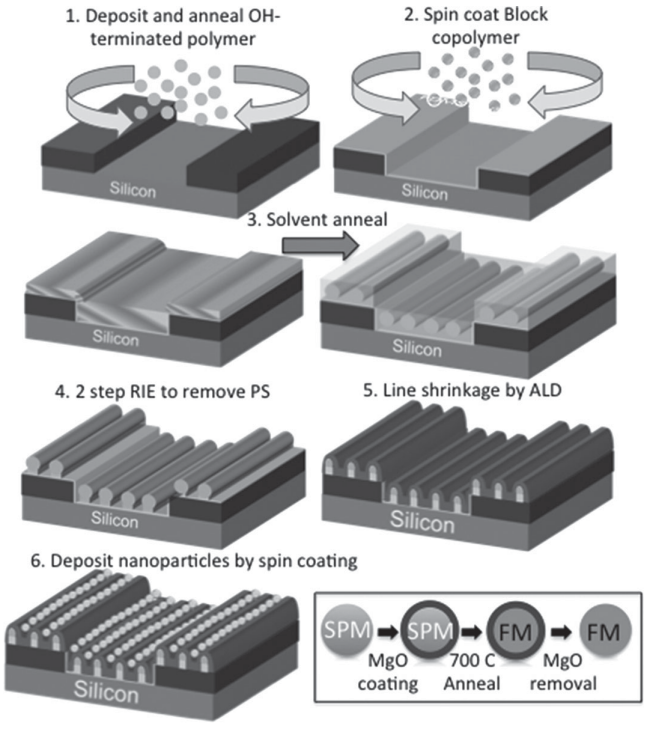

Scheme 1. Parts (1–6) show the process flow of the multiple step production of aligned nanocrystal patterns. The lower right section shows a schematic representation of the FePt nanoparticle synthesis.

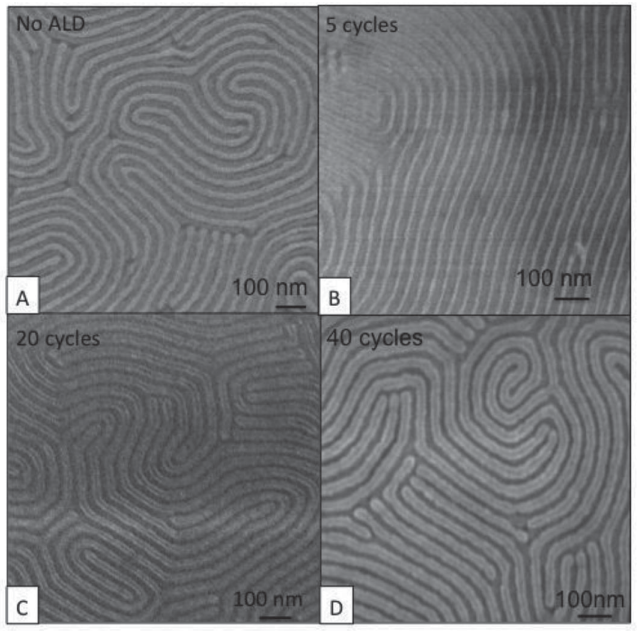

Figure 1. Characterization of the effect of ALD deposition on random BCP patterns. A) SEM image of a BCP pattern prior to ALD deposition. B–D) SEM images of similar patterns after 5, 20, and 40 ALD cycles, respectively. The trench width (L_s) is tuned controllably through this process.

is used to produce favorable interactions between the polymer and either a lithographically prepatterned or an unpatterned silicon wafer. The overall processing procedure for the films used in this study is summarized in **Scheme 1**. This process can be described by 6 steps: 1) spin coat the OH-terminated PDMS polymer onto the substrate and anneal; strip un-grafted polymer off the surface, 2) spin coat the BCP onto the PDMS coated surface, 3) solvent anneal the BCP to create a well ordered and well aligned structure, 4) use two-step reactive ion etch (RIE) to selectively remove the PS block, 5) shrink the lines using ALD deposition of alumina, and 6) deposit nanoparticles onto the patterned surface from solution. The first step in this process is crucial to create the self-assembled patterns described in this work. The use of an OH-terminated PDMS polymer is required to promote a polymer morphology composed of cylinders oriented parallel to the substrate. The grafted OH-terminated PDMS polymer also enhances wetting of the BCP film.[42] In step two, solvent annealing has been used here in preference over thermal annealing as it enhances both orientational and long-range translational order within the PS-*b*-PDMS system.

To create a physical pattern from the chemical (i.e., block copolymer) pattern, selective etching is needed. Jung et al. have previously shown that cylinder forming PS-*b*-PDMS block copolymer films with parallel orientations require a CF_4 RIE etch to first remove the PDMS over-layer and a subsequent O_2 RIE step to selectively remove the PS matrix to define the PDMS pattern.[42] **Figure 1**A shows a scanning electron microscopy (SEM) image of a random "fingerprint" PS-*b*-PDMS nanopattern after exposure to a CF_4 and O_2 plasma. The natural periodicity (L_0) of the pattern is 36 nm and the PDMS line dimension is approximately 16 nm ± 1 nm. Consequently, the spacing between the PDMS cylinders, designated L_s is 20 nm ± 1 nm which is too large to sequester 1D chains of nanoparticles.

To reduce the gap (L_s), we deposited ALD alumina with precise thicknesses directly onto the RIE etched polymer pattern. This allowed us to reduce the gap size conformally and with nanometer precision as shown in Figure 1. The SEM images show a bare pattern and patterns with 5 cycles, 20 cycles, and 40 cycles of ALD respectively. The original L_s value was ≈20 nm before alumina deposition and after 40 ALD cycles (corresponding to deposition of ≈4.5 nm of alumina), the L_s value was reduced to less than 10 nm. ALD deposition has been used previously to shrink the size of nanoscale inorganic features, including nanoscale Si features created using block co-polymer etch masks.[43] Selective ALD deposition has also been used to create physical patterns in unetched block co-polymer patterns.[44–46] Additionally, a similar process based on ALD, known as sequential infiltration synthesis (SIS) has been used to also create physical patterns in unetched block co-polymer patterns.[45,47] To the best of our knowledge, however, this work is the first example of applying ALD alumina deposition directly to an etched polymer pattern to change the physical structure.

In addition to our ability to tune the trench diameter, ALD deposition has many advantages in that it can transform a very unstable nanoscale pattern into a much more robust template for further nanoscale assembly. For example, the ALD step allows us to fill in small divots caused by nanometer level over-etching, a process which ensures that our finalized patterns are consistent from batch to batch. The ALD alumina layer also acts as a solvent protection layer that lets us deposit nanoparti-

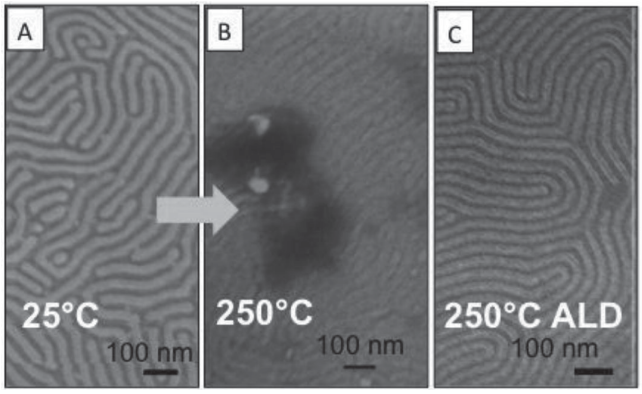

Figure 2. Characterization of the thermal stability of uncoated and alumina coated BCP nanopatterns. A) SEM image of the as synthesized BCP pattern. B) SEM image of the sample depicted in part a, after heating to 250 °C for 20 min. Clear degradation of the nanoscale structure is observed. C) SEM of a different piece of the sample shown in (A), this time heated to 250 °C after 20 cycles of ALD alumina deposition. Other than a decrease in the channel width caused by the alumina deposition, the pattern is well preserved.

cles onto the pattern from organic solvents that would normally dissolve or swell the block co-polymers, destroying the pattern. A final advantage to the ALD process is the added thermal stability of the patterns. **Figure 2** shows SEM images of an etched polymer pattern, that same pattern after heating to 250 °C for 25 min, and a sample with 20 cycles of ALD after heating to 250 °C for 25 min. Comparison between the original sample (Figure 2A) and the uncoated sample (Figure 2B) shows that there are large defects formed upon heating as well as reflow of the polymer as evidenced by reduction of the line spacing (L_s). Conversely comparison between the original sample (Figure 2A) and the ALD coated sample (Figure 2C) shows good retention of the morphology of the sample, other than the expected reduction in L_s due to the alumina coating.

2.2. Directed Self-Assembly

Random fingerprint patterns are excellent test structures for optimizing the ALD and NP deposition steps, but in order to study dipolar coupling between nanocrystals using bulk measurements, the magnetic nanoparticle arrays must have some form of uni-directional alignment. Block co-polymer nanopatterns can be aligned by various templating techniques, but for this work, physical epitaxy was chosen as the best way to create samples that are globally aligned on the centimeter scale, which is needed for SQuID magnetometry measurements.[1,16,48] **Figure 3**A shows an SEM image of a well-aligned PS-*b*-PDMS nanopattern deposited in a 300 nm trench in a Si wafer. An OH-terminated PDMS polymer was grafted to the silica surface of the wafer before deposition of the diblock co-polymer. The patterns were annealed for 4 h under a toluene:heptane vapor and received the same two-step RIE etch (35 s CF_4/25 s O_2) as the non-aligned samples shown in Figure 1 and 2. The lithographic trench spacing was optimized to be commensurate with the BCP nanopattern to ensure defects were not created by a mismatch. One key drawback with the physical epitaxy approach

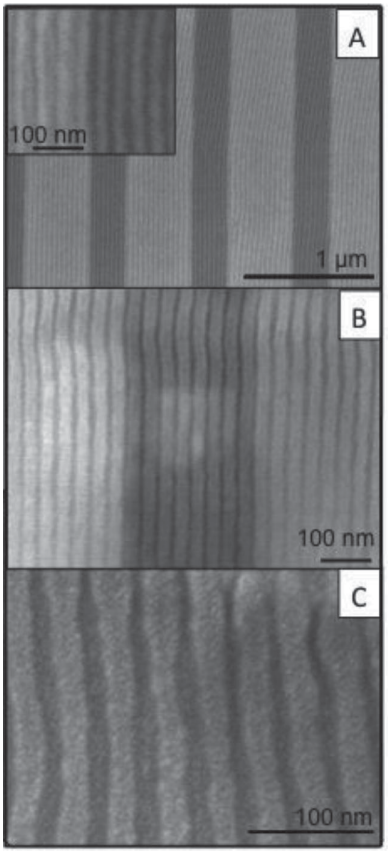

Figure 3. SEM images of the aligned BCP patterns with various coatings. A) The aligned polymer film after RIE. B) The nanopattern after 40 cycles of alumina ALD, resulting in a trench size of ≈10 nm. C) The nanopattern after ≈0.5 nm of Pt sputtered to the surface to create a non-oxidizing surface for the nanocrystals.

is the presence of the mesa and the large fraction of the total substrate area that it occupies. One could consider removing the polymer from the mesa or reducing its size,[49] but we chose instead to pattern both the trench and mesa regions with the same pattern to ensure that as much of the total substrate area as possible was patterned. Any unpatterned regions would likely result in nanoparticle agglomeration. However, the level of defects does increase when self-assembly occurs on both trench and mesa regions.

Here again, an ALD step was employed to reduce L_s to a value commensurate with the average nanoparticle size (7 nm as determined by transmission electron microscopy (TEM), **Figure 4**A,C). Figure 3B shows a SEM image of an ALD coated, aligned PS-*b*-PDMS pattern confined both within a trench and on top of the mesa. The original 19 nm gap was reduced by 10 nm using a 5nm deposition ALD step. The final L_s value is 9 nm, which is ideal for sequestering a nanoparticle of about 7 nm. Unfortunately, if the reactive, non-noble metal nanocrystals used here are deposited directly onto the alumina coating, they will be oxidized by the alumina, destroying the magnetic properties that make them interesting for this study. Therefore, a final coating step of less than 1 nm of Pt was needed to protect the FePt nanocrystals from oxidation. Figure 3C shows the patterns after a sputter coating of Pt. Some roughening of the

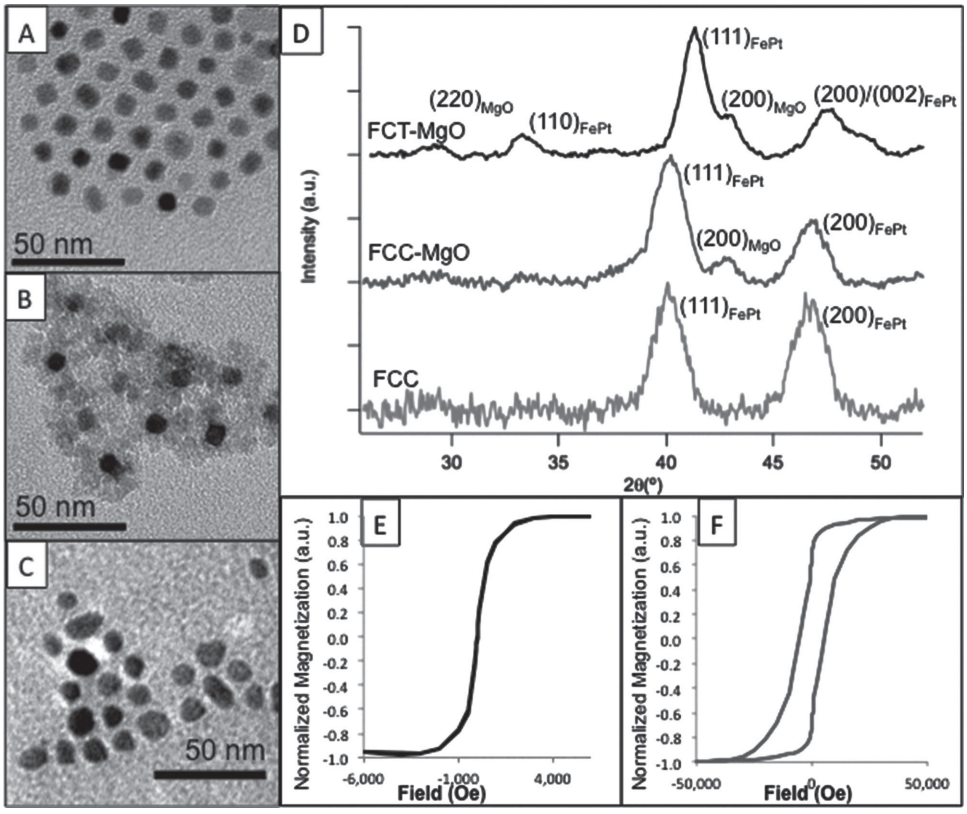

Figure 4. Characterization of FePt nanocrystals. A–C) TEM images of the as synthesized SPM nanocrystals, the SPM nanocrystals coated in MgO, and the final FM nanocrystals after the MgO is removed, as described in Scheme 1. D) Powder XRD data for samples similar to those shown in (A–C). The one exception is that the MgO is not removed from the fct nanocrystals for the diffraction experiment. Peaks form FePt and MgO are indexed on the figure. E,F) Magnetic hysteresis curves of the SPM/fcc and FM/fct magnetic nanocrystals, respectively, at 298 K.

surface occurs, but this roughness does not seem to prevent deposition of the nanocrystals onto the surface.

2.3. FCC Synthesis and FCT Conversion

Two different types of nanoparticles were used in this work and the synthesis of both types of nanocrystals has been reported previously.[50,51] The lower right panel of Scheme 1 summarizes the process used to synthesize those nanoparticles. Superparamagnetic (SPM) FePt nanocrystals were produced using a high temperature solution based decomposition of Fe and Pt precursors in the presence or organic capping ligands. SPM FePt nanocrystals were then converted to ferromagnetic (FM) FePt nanocrystals by individually coating the nanoparticles with MgO and then dry heating the MgO/FePt powder to drive the fcc to fct phase transition. Figure 4A shows a TEM image of the as synthesized SPM FePt and a TEM of the MgO coated SPM nanocrystals is shown in Figure 4B. Finally, the MgO was removed in solution and replaced with organic capping ligands (Figure 4C). Soluble, ligand capped versions of both the SPM and FM nanoparticles were then directly deposited on to the BCP patterns under inert conditions. Details about these processes can be found in the experimental section.

As discussed above, the SPM phase has a face centered cubic (fcc) structure, which is thermally converted to a magnetically hard (i.e., FM) phase with a face centered tetragonal (fct) structure. This conversion can then be confirmed by X-ray diffraction (XRD), as shown in Figure 4D. After coating with MgO the fcc structure is retained and there is an additional peak that corresponds to the MgO (200). After thermal conversion the FePt (200) peak splits to the (200)/(002) peaks and the fct (110) also becomes allowed, confirming the conversion from the fcc to the fct structure.

Sample magnetization as a function of applied magnetic field (i.e. magnetic hysteresis loops) were measured at room temperature for both the SPM and FM nanocrystals, as shown in Figure 4E,F, respectively. The magnetic measurements confirm that the as synthesized fcc nanoparticles are superparamagnetic. After thermal annealing the coercivity of the fct nanocrystals increases to 10 000 Oe and the ratio of the remanent magnetization to the saturation magnetization is 0.75, as expected in a ferromagnetic material.

The FM nanoparticles used were made from the same batch of SPM nanoparticles used in this study. This allowed consistency between the stoichiometry of the samples as well as the overall nanoparticle size and polydispersity. FM nanocrystals with larger coercive fields can be created with longer annealing times, but those nanocrystals quickly aggregate in solution and cannot be processed into the BCP trenches. Indeed, as seen below, the least aggregated and thus most solution processable fraction of this FM nanocrystal sample tends to show significantly smaller coercive fields than the sample average.

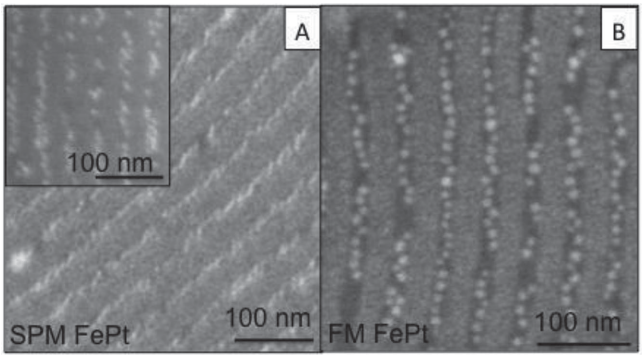

Figure 5. Characterization of magnetic nanoparticles in aligned BCP patterns. A) Arrangement of SPM FePt nanocrystals and b) FM FePt nanocrystals, both organized into mostly 1D chains. The inset (A) shows that some cannels in this sample are big enough to accommodate double rows of nanocrystals, even though the majority of the sample contains single chains.

2.4. Directed Deposition/Placement of NPs within BCP Patterns

Nanoparticle deposition was achieved by spin-coating semi-dilute (≈0.1–1 mg mL^{-1}) solutions of nanoparticles from chloroform at high spin speeds (i.e., 9000 rpm) onto aligned PS-*b*-PDMS patterns. It has been shown previously that during spin coating of colloidal solutions onto trenched surfaces, both solvent and colloids become trapped in the trenches while excess solvent and colloids are flung off the sample.[35] Because of this, upon solvent evaporation, clean arrays of colloids trapped in the trenches can be created. **Figure 5**A,B show SEM images of the SPM and FM nanocrystals, respectively, deposited onto the aligned substrates, as described above. Nanocrystal deposition from solution in this manner gives almost full coverage of the substrates with 1D nanocrystal chains. As shown in the inset of Figure 5A,B, however, there are many breaks where the chains are not complete, so this system cannot be considered to contain infinite 1D coupling. The inset also shows that there are a few regions where the trenches are wider and nanoparticles stack 2 and 3 particles across.

Despite the defects shown in the Figure 5A inset, the images in Figure 5A,B make it clear that the majority of the population contains 1D nanocrystal chains. This is one of the benefits of the processing steps described previously: the ability to tune the number of nanocrystals in each trench and specifically to create trenches that trap 1D chains of nanocrystals. If fewer ALD cycles were used, one should be able to create zigzag and dimer chains of particles, as shown previously using trenches of different diameters.[52]

2.5. Magnetometry Analysis of Coupled Nanoparticles

Magnetic measurements were performed on the samples similar to those shown in Figure 5, with the exception that the samples were capped with 25 nm of Au to prevent oxidation. To study the coupling between magnetic nanocrystals in chains, magnetization was measured with the unique axis of BCP patterns oriented both parallel and perpendicular to the applied magnetic field. **Figure 6**A shows magnetic moment (M) measurements as a function of applied magnetic field at 20 K for the fcc/SPM sample. This temperature is below the SPM-to-FM transitions for these nanocrystals; we chose this temperature so that we could measure coupling between fixed magnetic dipoles for chains nanoparticles produced by the BCP pattern. This coupling is expected to be washed out by thermal fluctuations at room temperature. The fcc/SPM particles have a coercivity of 200 Oe at 20 K, confirming their ferromagnetic nature. When the samples are measured with the applied field parallel to the trench axis, the magnetic saturation is increased by 33%, compared to measurements made perpendicular to the chains. This enhancement in magnetization arises from the creation of a magnetic easy axis along the trench direction. The symmetry breaking that causes this new easy axis confirms magnetic coupling along the nanocrystal chains.

Similarly, Figure 6B shows room temperature magnetization measurements made on the fct/FM nanocrystals. The samples show a coercivity of 800 Oe, confirming that these samples are ferromagnetic. Similar to the SPM particles, the samples show an enhancement of the saturation magnetization of 35% when measured with the applied field parallel to the channels compared to the saturation magnetization measure with the applied field perpendicular to the channel direction. This anisotropy again indicates the creation of a magnetic easy axis along the channel direction due to coupling between magnetic nanocrystals.

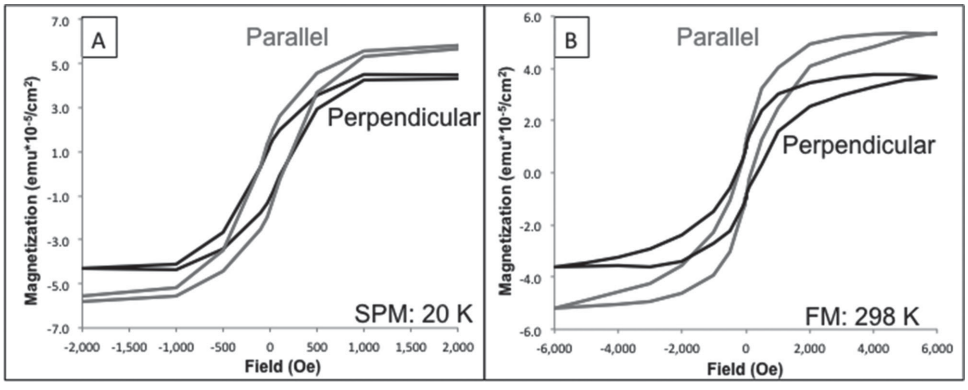

Figure 6. Magnetic hysteresis curves obtained on aligned substrates. A) SPM nanocrystals measured at 20 K. B) FM nanocrystals measured at 298 K. Samples were measured with the magnetic field applied along the trenches (parallel), and orthogonal to the trenches (perpendicular). In both cases, dipole-dipole coupling between nanocrystals creates an array with a preference for magnetization oriented parallel to the channel axis.

All samples clearly show magnetic anisotropy that correlates with the structural anisotropy seen in Figure 5. The difference in the saturation magnetization measured parallel to the channel axis is less than a factor of 2× greater than that measured perpendicular to the channel axis, however. The magnetic anisotropy is likely limited by multiple factors. Disorder in the chains should frustrate coupling. Thermal fluctuations of the magnetic dipoles could further limit coupling. Probably most importantly, however, is the fact that the nanocrystals were deposited by spin coating, which involves fast evaporation of the solvent. Under these deposition conditions, there may not be sufficient driving force to fully align the unique magnetic axis of the nanocrystals with the channel axis. The result would be magnetocrystalline anisotropy that competes with dipole-dipole coupling, reducing the overall anisotropy. While the magnetic anisotropy is modest in these samples, all films show distinct magnetic anisotropy, indicating coupling between magnetic nanocrystals in chains.

3. Conclusion

Self-assembled trench arrays were made using diblock co-polymers with one easily etchable block. Random fingerprint patterns were made on flat substrates and straight aligned patterns were produced by deposition into lithographically generated tranches. We have further shown that we can tune the trench size (L_s) by precise ALD alumina deposition. The ALD process is beneficial as it makes the patterns more thermally robust and it protects the patterns from solvents needed in later processing steps. This process results in a global alignment of trenches with tunable size and surface composition.

These substrates create an ideal platform to study the coupling of magnetic nanoparticle arrays. Here we used both superparamagnetic and ferromagnetic FePt nanocrystals. We showed that linear arrays of nanocrystals could be produced using trenches that were size matched to the nanocrystals. The nanocrystal arrays showed magnetic coupling along the chains of nanocrystals suggesting that this process can be used to create interacting magnetic nanoparticle arrays. Similar arrays may eventually find applications in devices that rely on unidirectional coupling between nanomagnetic domains.

4. Experimental Section

Materials: For the FePt synthesis iron pentacarbonyl (98%, Aldrich), oleic acid (90%, Aldrich), oleylamine (>70%, Aldrich), 1-octadecene (90%, Aldrich), 1,2-tetradecanediol (98%, Aldrich), Pt(acetylacetonate)$_2$ (98%, Strem), Mg(acetylacetonate)$_2$ (98%, Strem), and hexadecanethiol (90%, Alfa Aesar) were used as received without further purification.

All hydroxyl-terminated homopolymer and the diblock co-polymer were supplied from Polymer Source, Inc. and were used as received. The initial layer was hydroxy-terminated polydimethylsiloxane with a molecular weight of 5.3 kg mol^{-1}. The diblock co-polymer was a cylinder-forming poly(styrene)-block-poly(methyl methacrylate) (PS-*b*-PDMS) with a total M_w of 42.0 kg mol^{-1}, a PS M_w of 34.0 kg mol^{-1}, a PDMS M_w of 11.0 kg mol^{-1}, and a PDI ≤ 1.1.

FCC/FCT FePt Nanocrystal Synthesis: Synthesis of ≈7 nm SPM, FePt nanocrystals is based on previously published methods.[50,51] Briefly, a solution containing Pt(acetylacetonate)$_2$ (0.5 mmol), 1-ocatadecene (10 mL), oleic acid (4 mmol), and oleylamine (4 mmol) was stirred in a 250 mL three-neck flask under a gentle argon flow. The solution was then heated to 120 °C at a rate of 6 °C min^{-1}. This temperature was held for 13 min to insure full dissolution of the Pt precursor. At this point iron pentacarbonyl (0.20 mL) was added. The solution was then heated to 240 °C at a ramp rate of 3 °C min^{-1} and refluxed at 240 °C for 1 h . Finally, the solution was cooled and the particles were precipitated with ethanol and centrifuged. Two further washings were done with ethanol and hexane followed by centrifugation. The particles were then dispersed in hexane (10 mL).

Synthesis of MgO Coated SPM-FePt Nanocrystals: This synthesis again utilizes previously published methods.[50,51] A solution containing Mg(acetylacetonate)$_2$ (2 mmol), tetradecanediol (4 mmol), oleic acid (4 mmol), oleyamine (4 mmol), and benzyl ether (20 mL) was stirred in a 250 mL three-neck flask under gentle argon flow. The solution was first heated to 80 °C and held at this temperature to insure dissolution of the precursors. Next the FePt particle solution (5 mL) obtained above was rapidly (within 2 s) injected into the flask. The solution was then heated to 120 °C and held for 20 min to insure that all of the hexane was removed. Finally, the solution was quickly heated to 298 °C and refluxed at that temperature for 1 h. The particles were collected and purified via the same procedure described above.

Self-Assembly of the PS-b-PDMS Nanopatterns: All silicon substrates were cleaned in fresh piranha solution (3:1 concentrated sulfuric acid to 30% hydrogen peroxide) at 85 °C for 1 h. The OH-terminated PDMS polymer was deposited from a 1.5% weight solution onto silicon via spin coating and was grafted to the native oxide by annealing at 150 °C for 16 h under vacuum. The un-grafted OH-terminated PDMS polymer layers were removed by sonication in toluene.[42] The PS-*b*-PDMS diblock co-polymer used here has a natural periodicity (L_0) of 36 nm. To appropriately match this periodicity, BCP films with a final thickness of 40–45 nm were cast from 0.5% weight solutions in carbon-tetra-chloride by spin coating at 6000 rpm for 20 s. The block co-polymer patterns were solvent annealed in a vapor of toluene and heptane (using a solution with a volume ratio of 3.5:1 toluene:heptane to generate the solvent) for a period of 4 h. The nanopatterns were developed using a two-step reactive-ion etching (RIE) process on a STS AOE etcher to first remove the PDMS over-layer (CF_4, 100W) and next to selectively remove the PS matrix (O_2, 100W).[42]

Directed Self-Assembly of the PS-b-PDMS Nanopatterns: Patterned silicon substrates with a native surface oxide layer were used for graphoepitaxial alignment of the PS-PDMS patterns.[1,16] The final dimensions of lithographic trenches used in this work were 300–400 nm wide, 35–45 nm deep, with a pitch of 900 nm. The total patterned area of each sample 6 mm × 6 mm. This size was chosen to ensure that the self-assembly methods used here were scaleable to macroscopic dimensions and to provide ideal sampling for SQuID measurements. The PS-*b*-PDMS patterns were deposited, solvent annealed and etched on the patterned wafers using the same parameters outlined in the previous sections.

ALD Al_2O_3 Nanogap Reduction and Pt-Sputtering: Atomic layer deposition (ALD) of amorphous alumina (Al_2O_3) was performed in a Savannah 100 from Cambridge NanoTech Inc. operating at 250 °C and 20 mTorr. Trimethylaluminum and H_2O were used as the sources of aluminum and oxygen, respectively, and a 20 sccm continuous nitrogen flow rate was used throughout the deposition. The deposition rate of Al_2O_3 was 0.11 nm per cycle (i.e., 10 cycles = 1.1 nm). Based on the PDMS cylinder-to-cylinder spacing, the conformal coating was tuned to be commensurate with the nanoparticle size. Pt sputtering was done using a Hummer 6.2 from Anatech.

NP Release and Deposition: The MgO coated SPM-FePt, nanocrystals were heated in a tube oven at 750 °C under a flow of 5% hydrogen gas and 95% argon gas for 3 h to convert them to the FM fct crystal structure. The heated powders were then washed with a two-phase solution containing aqueous HCl (10% vol) and a chloroform solution made by mixing 20 mL of chloroform 5 drops of hexadecanethiol and 5 drops of oleic acid.[50,51] The vial was sonicated for ≈10 min and then shaken for 30 min. The dispersed MgO-free FM-FePt particles were collected from the chloroform layer and spun onto the patterned substrates from this solution.

SPM and FM nanoparticles were deposited via spin-coating in an argon filled glove box to minimize oxidation of the nanoparticle arrays. Both SPM and FM nanoparticles were deposited at 8000 rpm from chloroform solutions onto the Pt/ALD-coated, etched PS-*b*-PDMS nanopatterns. Samples were protected from oxidation for magnetometry measurements by depositing a thin Au coating (≈25 nm) via thermal evaporation onto the nanocrystal arrays. Samples were further sealing using kapton tape before being removed from the argon atmosphere.

Characterization: Wide angle X-ray scattering (WAXS) measurements were carried out on a Bruker D8-GADDS diffractometer (Cu Kα radiation). SEM was performed on a JEOL JSF6700 with a semi in-lens detector operating at an accelerating voltage of 3 kV. All samples were imaged without any additional metallic coatings. Low-resolution TEM was performed using an FEI CM120 system operating at 120 kV. A Quantum Design MPMS superconducting quantum interference device (SQuID) magnetometer was used to measure hysteresis loops and remanence curves at various temperatures.

Acknowledgements

The authors wish to thank Dr. Ignacio Martini for assistance with SQuID magnetometry and SEM. They also thank Guangye Zhang for help with Au evaporation and spin coating. This work was supported by the National Science Foundation under Cooperative Agreement Award EEC-1160504 which funds TANMS, an NERC focused on Translational Aspects of Nanoscale Multiferroic Materials. Initial support for this project was provided by the Western Institute of Nanoelectronics, which was sponsored by NERC (NRI), Intel, and the UC Discovery Program. The authors acknowledge the use of instruments at the Electron Imaging Center for NanoMachines supported by the NIH (grant 1S10RR23057 to ZHZ) at the California NanoSystems Institute, UCLA.

Received: June 12, 2014
Revised: July 16, 2014
Published online: September 1, 2014

[1] S. B. Darling, *Prog. Polym. Sci.* **2007**, *32*, 1152.
[2] H.-C. Kim, S.-M. Park, W. D. Hinsberg, *Chem. Rev.* **2010**, *110*, 146.
[3] C. T. Black, R. Ruiz, G. Breyta, J. Y. Cheng, M. E. Colburn, K. W. Guarini, Y. Zhang, *IBM J. Res Dev.* **2007**, *51*, 605.
[4] M. Park, C. Harrison, P. M. Chaikin, R. A. Register, D. H. Adamson, *Science* **1997**, *276*, 1401.
[5] T. Thurn-Albrecht, J. Schotter, G. A. Kastle, N. Emley, T. Shibauchi, L. Krusin-Elbaum, K. Guarini, C. T. Black, M. T. Tuominen, T. P. Russell, *Science* **2000**, *290*, 2126.
[6] R. A. Segalman, H. Yokoyama, E. J. Kramer, *Adv. Mater.* **2001**, *13*, 1152.
[7] S. Ludwigs, A. Böker, A. Voronov, N. Rehse, R. Magerle, G. Krausch, *Nat. Mater.* **2003**, *2*, 744.
[8] S. O. Kim, H. H. Solak, M. P. Stoykovich, N. J. Ferrier, J. J. De Pablo, P. F. Nealey, *Nature* **2003**, *424*, 411.
[9] M. P. Stoykovich, M. Müller, S. O. Kim, H. H. Solak, E. W. Edwards, J. J. de Pablo, P. F. Nealey, *Science* **2005**, *308*, 1442.
[10] J. Chai, D. Wang, X. Fan, J. M. Buriak, *Nat. Nanotechnol.* **2007**, *2*, 500.
[11] C. Tang, E. M. Lennon, G. H. Fredrickson, E. J. Kramer, C. J. Hawker, *Science* **2008**, *322*, 429.
[12] S. Park, D. H. Lee, J. Xu, B. Kim, S. W. Hong, U. Jeong, T. Xu, T. P. Russell, *Science* **2009**, *323*, 1030.
[13] S.-J. Jeong, G. Xia, B. H. Kim, D. O. Shin, S.-H. Kwon, S.-W. Kang, S. O. Kim, *Adv. Mater.* **2008**, *20*, 1898.
[14] S. O. Kim, B. H. Kim, D. Meng, D. O. Shin, C. M. Koo, H. H. Solak, Q. Wang, *Adv. Mater.* **2007**, *19*, 3271.
[15] R. Ruiz, H. Kang, F. A Detcheverry, E. Dobisz, D. S. Kercher, T. R. Albrecht, J. J. de Pablo, P. F. Nealey, *Science* **2008**, *321*, 936.
[16] I. Bita, J. K. W. Yang, Y. S. Jung, C. A Ross, E. L. Thomas, K. K. Berggren, *Science* **2008**, *321*, 939.
[17] S.-J. Jeong, J. E. Kim, H.-S. Moon, B. H. Kim, S. M. Kim, J. B. Kim, S. O. Kim, *Nano Lett.* **2009**, *9*, 2300.
[18] J. Y. Cheng, D. P. Sanders, H. D. Truong, S. Harrer, A. Friz, S. Holmes, M. Colburn, W. D. Hinsberg, *ACS Nano* **2010**, *4*, 4815.
[19] J. Y. Cheng, C. A. Ross, E. L. Thomas, H. I. Smith, G. J. Vancso, *Adv. Mater.* **2003**, *15*, 1599.
[20] J. Y. Cheng, A. M. Mayes, C. A. Ross, *Nat. Mater.* **2004**, *3*, 823.
[21] S.-M. Park, M. P. Stoykovich, R. Ruiz, Y. Zhang, C. T. Black, P. F. Nealey, *Adv. Mater.* **2007**, *19*, 607.
[22] S. Sun, *Adv. Mater.* **2006**, *18*, 393.
[23] M. Chen, D. E. Nikles, H. Yin, S. Wang, J. W. Harrell, S. A. Majetich, *J. Magn. Magn. Mater.* **2003**, *266*, 8.
[24] J. J. Benkoski, J. L. Breidenich, O. M. Uy, A. T. Hayes, R. M. Deacon, H. B. Land, J. M. Spicer, P. Y. Keng, J. Pyun, *J. Mater. Chem.* **2011**, *21*, 7314.
[25] B. Y. Kim, I.-B. Shim, O. L. A. Monti, J. Pyun, *Chem. Commun.* **2011**, *47*, 890.
[26] S. Sun, C. B. Murray, D. Weller, L. Folks, A. Moser, *Science* **2000**, *287*, 1989.
[27] N. Sharma, G. H. Jaffari, S. I. Shah, D. J. Pochan, *Nanotechnology* **2010**, *21*, 85707.
[28] L. Zhang, A. Manthiram, *Phys. Rev. B. Condens. Matter* **1996**, *54*, 3462.
[29] S. Y. Chou, M. S. Wei, P. R. Krauss, P. B. Fischer, *J. Appl. Phys.* **1994**, *76*, 6673.
[30] C. A. Ross, H. I. Smith, T. Savas, M. Schattenburg, M. Farhoud, M. Hwang, M. Walsh, M. C. Abraham, R. J. Ram, *J. Vac. Sci. Technol. B* **1999**, *17*, 3168.
[31] S. A. Morin, Y.-H. La, C.-C. Liu, J. A. Streifer, R. J. Hamers, P. F. Nealey, S. Jin, *Angew. Chemie* **2009**, *48*, 2135.
[32] A. Haryono, W. H. Binder, *Small* **2006**, *2*, 600.
[33] S. B. Darling, N. A. Yufa, A. L. Cisse, S. D. Bader, S. J. Sibener, *Adv. Mater.* **2005**, *17*, 2446.
[34] S. B. Darling, S. D. Bader, *J. Mater. Chem.* **2005**, *15*, 4189.
[35] S. B. Darling, *Surf. Sci.* **2007**, *601*, 2555.
[36] O. Gutfleisch, J. Lyubina, K.-H. Muller, L. Schultz, *Adv. Eng. Mater.* **2005**, *7*, 208.
[37] Z. R. Dai, S. Sun, Z. L. Wang, *Nano Lett.* **2001**, *1*, 443.
[38] S.-Y. Bae, K.-H. Shin, J.-Y. Jeong, J.-G. Kim, *J. Appl. Phys.* **2000**, *87*, 6953.
[39] M. Delalande, M. J. -F. Guinel, L. F. Allard, A. Delattre, R. Le Bris, Y. Samson, P. Bayle-Guillemaud, P. Reiss, *J. Phys. C Solid State Phys.* **2012**, *116*, 6866.
[40] A. Moser, K. Takano, D. T. Margulies, M. Albrecht, Y. Sonobe, Y. Ikeda, S. Sun, E. E. Fullerton, *J. Phys. D. Appl. Phys.* **2002**, *35*, R157.
[41] N. A. Frey, S. Peng, K. Cheng, S. Sun, *Chem. Soc. Rev.* **2009**, *38*, 2532.
[42] Y. S. Jung, C. A. Ross, *Nano Lett.* **2007**, *7*, 2046.
[43] A. Andreozzi, L. Lamagna, G. Seguini, M. Fanciulli, S. Schamm-Chardon, C. Castro, M. Perego, *Nanotechnology* **2011**, *22*, 335303.
[44] Q. Peng, Y.-C. Tseng, S. B. Darling, J. W. Elam, *Adv. Mater.* **2010**, *22*, 5129.
[45] M. Ramanathan, Y.-C. Tseng, K. Ariga, S. B. Darling, *J. Mater. Chem. C* **2013**, *1*, 2080.
[46] C. A. Wilson, R. K. Grubbs, S. M. George, *Chem. Mater.* **2005**, *17*, 5625.
[47] J. Yin, Q. Xu, Z. Wang, X. Yao, Y. Wang, *J. Mater. Chem. C* **2013**, *1*, 1029.
[48] B. C. Berry, G. Singh, H.-C. Kim, A. Karim, *ACS Macro Lett.* **2013**, *2*, 346.
[49] D. Sundrani, S. B. Darling, S. J. Sibener, *Langmuir* **2004**, *20*, 5091.
[50] J. Kim, C. Rong, Y. Lee, J. P. Liu, S. Sun, *Chem. Mater.* **2008**, *20*, 7242.
[51] J. Kim, C. Rong, J. P. Liu, S. Sun, *Adv. Mater.* **2009**, *21*, 906.
[52] K. Xu, L. Qin, J. R. Heath, *Nat. Nanotechnol.* **2009**, *4*, 368.